

1 **A seismic analysis of subglacial lake D2 (Subglacial Lake Cheongsuk)**
2 **beneath David Glacier, Antarctica**

3 Hyeontae Ju^{1,2}, Seung-Goo Kang³, Yeonjin Choi³, Sukjoon Pyun², Min Je Lee³, Hoje Kwak⁴, Kwansoo
4 Kim¹, Yeadong Kim⁵, Jong Ik Lee³

5 ¹Center of Technology Development, Korea Polar Research Institute, Incheon 21990, Korea

6 ²Department of Energy Resource Engineering, Inha University, Incheon 22212, Korea

7 ³Division of Glacier & Earth Sciences, Korea Polar Research Institute, Incheon 21990, Korea

8 ⁴Unit of Antarctic Inland Research, Korea Polar Research Institute, Incheon 21990, Korea

9 ⁵Korea National Committee on Polar Research, Incheon 21990, Korea

10

11 *Correspondence to:* Seung-Goo Kang (ksg9322@kopri.re.kr)

12 **Abstract.** Subglacial lakes beneath Antarctic glaciers are pivotal in advancing our understanding of cryosphere dynamics,
13 basal hydrology, and microbial ecosystems. We investigate the internal structure and physical properties of Subglacial Lake
14 D2 (SLD2), which is located beneath David Glacier in East Antarctica, using seismic data acquired during the 2021/22 austral
15 summer. The dataset underwent a comprehensive processing workflow, including noise attenuation, velocity analysis, and
16 prestack time migration. The migrated seismic sections revealed distinct reverse-polarity reflections at the glacier–lake
17 interface; however, reflections from the lake–bed sediment interface were ambiguous, leading to interpretational uncertainty
18 about the presence of a sediment layer. To resolve this interpretational uncertainty, two alternative structural models were
19 established: Model 1 (no sediment) and Model 2 (with a sediment layer). Synthetic seismograms generated by wave-
20 propagation modeling were compared with field data to validate the subglacial lake structure. The results confirmed the water
21 column thickness to be approximately 82 m (Model 1) or approximately 10 m (Model 2), and possible structural scenarios for
22 the subglacial lake were presented. Additionally, discontinuous reflections detected in seismic sections transverse to the ice
23 flow were interpreted as scour-like feature surfaces formed by ice movement. This study identified the basal structure beneath
24 the subglacial lake, which had been challenging to identify with conventional radar surveys, through seismic surveying. In
25 addition, ambiguous signals in the field seismic data were mitigated via quantitative comparison with synthetic data, thereby
26 facilitating interpretation of the underlying structure. Collectively, these findings enhance our understanding of subglacial lake
27 environments and inform the selection of future drilling sites for in situ sampling.

28 **1 Introduction**

29 Subglacial lakes beneath the Antarctic ice sheet are typically overlain by glaciers several kilometers thick and have remained
30 isolated from direct atmospheric and solar influences for millions of years, creating extreme environments characterized by
31 low temperatures (Thoma et al., 2010) and high pressures (Tulaczyk et al., 2014). With increasing scientific interest, subglacial

32 lakes have become a focal point for studies related to the Antarctic paleoclimate, as inferred from lake sediments, as well as
33 investigations into microbial life in polar ecosystems (Bell et al., 2007, 2011; Bentley et al., 2009; Christner et al., 2014;
34 Engelhardt et al., 1990; Priscu and Christner, 2003; Rose, 1979; Wingham et al., 2006). Subglacial lakes in Antarctica are
35 generally categorized as either stable or active. Approximately 80% of subglacial lakes in Antarctica are classified as stable
36 subglacial lakes. These closed systems do not exhibit significant surface elevation changes and are characterized by long-term
37 balance between recharge and discharge, although the extent of subglacial water exchange remains uncertain in the absence of
38 direct observations. The remaining 20% are classified as active subglacial lakes, which exhibit surface elevation changes due
39 to episodic water drainage and refilling events (Livingstone et al., 2022). Such active lakes can reduce basal friction as they
40 expand, thereby facilitating glacier flow and, in some cases, accelerating calving processes, ultimately influencing glacier
41 dynamics (Bell et al., 2007; Stearns et al., 2008; Winsborrow et al., 2010). Characterizing subglacial lakes is essential for
42 understanding cryospheric processes, reconstructing past climate conditions, and assessing the potential for life in isolated,
43 extreme environments.

44 The sampling of subglacial lake water, sediments, and microbial communities is critical to address these scientific objectives.
45 However, successful sampling requires careful selection and characterization of the drilling site. Airborne ice-penetrating radar
46 (IPR) surveys are commonly employed at regional scales to detect potential subglacial lakes suitable for drilling (Christianson
47 et al., 2012; Lindzey et al., 2020; Yan et al., 2022). However, due to signal attenuation in water, IPR surveys are limited in
48 resolving the internal structure of subglacial lakes. To overcome this limitation, seismic surveys have been conducted at
49 potential subglacial lake candidates identified from IPR surveys. During such surveys, P-waves propagate through the water
50 column and are partially reflected at the lake–bed interface because of contrasts in acoustic impedance. Analyzing these
51 reflected waves enables detailed delineation of the water column and underlying substrate, thereby informing optimal drilling
52 locations (Brisbourne et al., 2023; Filina et al., 2008; Horgan et al., 2012; Woodward et al., 2010).

53 As such, numerous studies have utilized seismic surveys to investigate the characteristics of subglacial lakes, including
54 Subglacial Lake Ellsworth, Subglacial Lake Whillans, and Subglacial Lake CECs. Subglacial Lake Ellsworth, located beneath
55 2,930–3,280 m of glacial ice in West Antarctica, was the subject of a seismic survey during the austral summer of 2007–08.
56 This survey revealed spatially variable ice thickness and a lake water column ranging from 52 to 156 m, which guided the
57 identification of an optimal drilling location (Smith et al., 2018; Woodward et al., 2010). Subglacial Lake Whillans lies beneath
58 approximately 800 m of ice. Seismic observations conducted during the 2010/11 field season revealed water columns
59 extending over a 5 km segment of the survey profile, with a maximum thickness of less than 8 m. The glacier bed was
60 predominantly composed of soft sediments, and localized zones with shallow water columns (< 2 m) were also identified
61 (Horgan et al., 2012). Subsequent drilling in the summer of 2012/13 confirmed the presence of microbial life in both the water
62 and sediment samples (Christner et al., 2014). Subglacial Lake CECs (SLCECs), located beneath 2653 m of ice at the Rutford–
63 Institute–Minnesota Divide in West Antarctica, were investigated through seismic surveys conducted in the 2016/17 and
64 2021/22 seasons. These surveys revealed a maximum water column thickness of 301.3 ± 1.5 m and clastic sediments up to 15

65 m thick covering the lakebed. While the lake center was relatively flat, significant topographic variability was observed near
66 the lake margins (Brisbourne et al., 2023).

67 We have initiated subglacial lake research beneath David Glacier, the closest major glacier to Jang Bogo Station in East
68 Antarctica. Satellite altimetry has identified six subglacial lakes in this region (Smith et al., 2009; Wright and Siegert, 2012).
69 During the 2016/17 austral summer, an airborne IPR survey was conducted over the region encompassing Subglacial Lake D1
70 (SLD1) and Subglacial Lake D2 (SLD2) (Lindzey et al., 2020). A subsequent high-resolution IPR survey was carried out
71 during the 2018/19 field season, focusing solely on SLD2 (also referred to as “Subglacial Lake Cheongsuk”) (Ju et al., 2025).
72 Ju et al. (2025) subdivided the previously identified single subglacial water body at SLD2, as detected by ICESat altimetry,
73 into three smaller subglacial lakes: SLD2-A, SLD2-B, and SLD2-C. Among these, SLD2-A represents the largest areal extent,
74 and targeted seismic surveys were conducted over this area to obtain high-resolution information on the lake depth and basal
75 structure. In the 2019/20 season, an initial seismic campaign identified the glacier thickness and suggested the presence of the
76 lake; however, the data quality was compromised by surface crevasse noise and a lack of adequate fold coverage, limiting
77 detailed interpretation. A refined seismic survey with 8-fold coverage was conducted during the 2021/22 season to address
78 these issues. Furthermore, the sound source was positioned further from the crevasse (end-shot), delaying the arrival of
79 crevasse-generated noise and preventing it from obscuring key reflections.

80 In this study, we present a detailed analysis of the physical and structural properties of SLD2-A using seismic data acquired
81 during the 2021/22 campaign. We first describe the seismic data processing workflow, including noise attenuation, amplitude
82 correction, and prestack time migration. Some areas of the processed field seismic data are challenging to interpret due to a
83 lack of subsurface information, overlap with ghost signals, and signal attenuation. In the case of the SLD2 region, the absence
84 of borehole data introduces inherent uncertainty into the subglacial lake structure derived from the Prestack Time Migration
85 (PSTM) section. In particular, reflections associated with the sediment layer are challenging to interpret because they have
86 weak amplitudes and overlap with ghost components. To compensate for these limitations, a subsurface structural model was
87 constructed, and model-based synthetic seismograms were compared and analyzed against field observations. As a result, the
88 substructure of SLD2-A is quantitatively presented as two possible scenarios: Glacier–Lake–Bedrock (model 1) or Glacier–
89 Lake–Sediment–Bedrock (model 2).

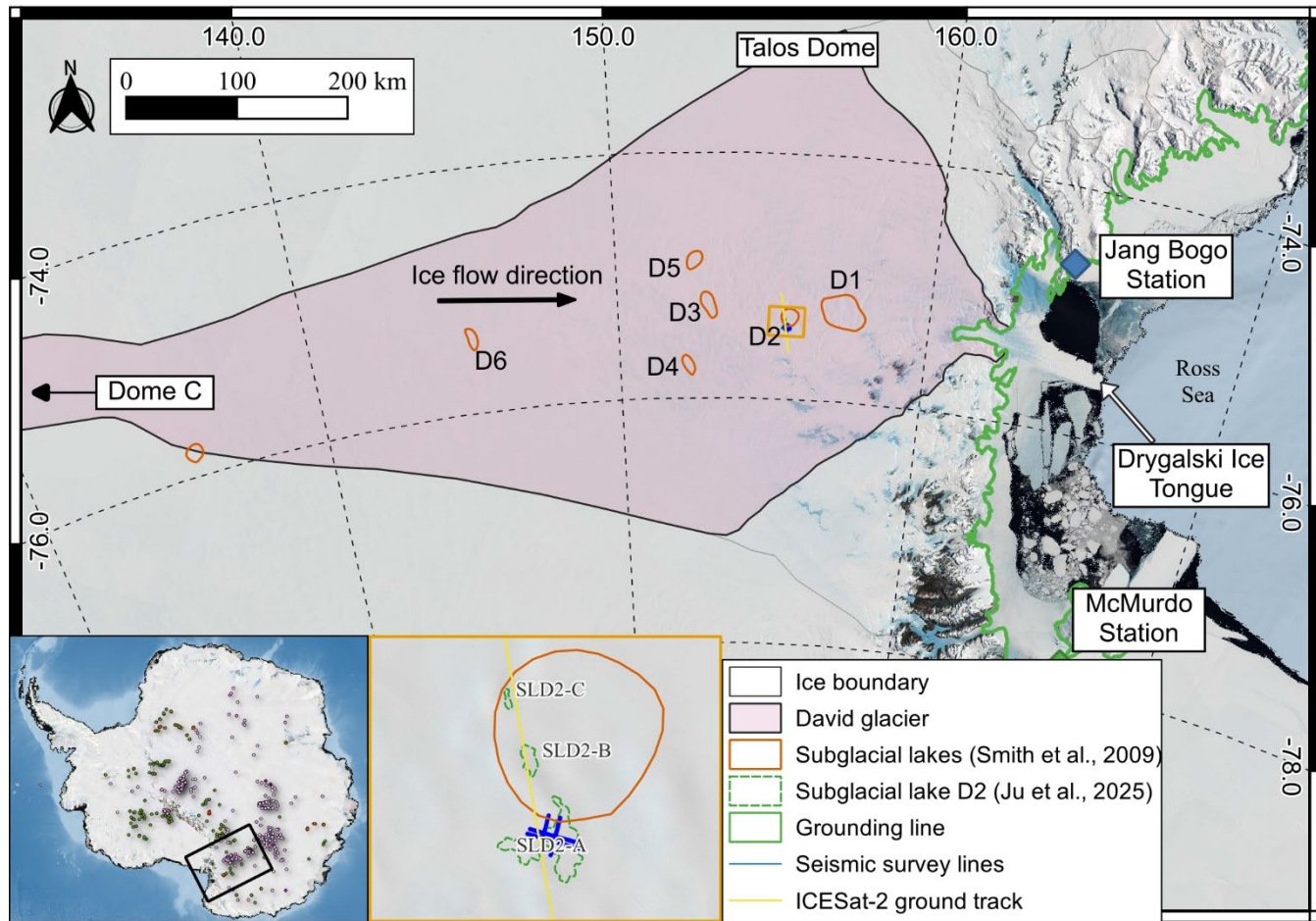
90 **2 Subglacial Lake D2 Beneath David Glacier in Antarctica**

91 **2.1 David Glacier**

92 David Glacier, located in Victoria Land, East Antarctica, originates from the Dome C and Talos Dome regions and flows
93 seaward through the Drygalski Ice Tongue (Fig. 1). The mass balance of glaciers from 1979 to 2008 has been estimated at $7.5 \pm 0.4 \text{ Gt yr}^{-1}$ (Rignot et al., 2019), while the mean ice discharge over the more extended period from 1979 to 2017 was reported
94 to be approximately 9.7 Gt yr^{-1} (Frezzotti et al., 2000; Rignot et al., 2019). According to Smith et al. (2020), satellite altimetry
95 observations from ICESat-1 and ICESat-2 (2003–2019) indicate that the grounded portion of David Glacier experienced a mass
96

97 gain of 3 ± 2 Gt yr $^{-1}$, whereas the adjacent ice shelves exhibited a mass loss of -1.6 ± 1 Gt yr $^{-1}$. Although the overall mass
98 balance of David Glacier currently appears stable, several active subglacial lakes observed by satellites have the potential to
99 influence glacier dynamics (Ju et al., 2025; Kim et al., 2025).

100



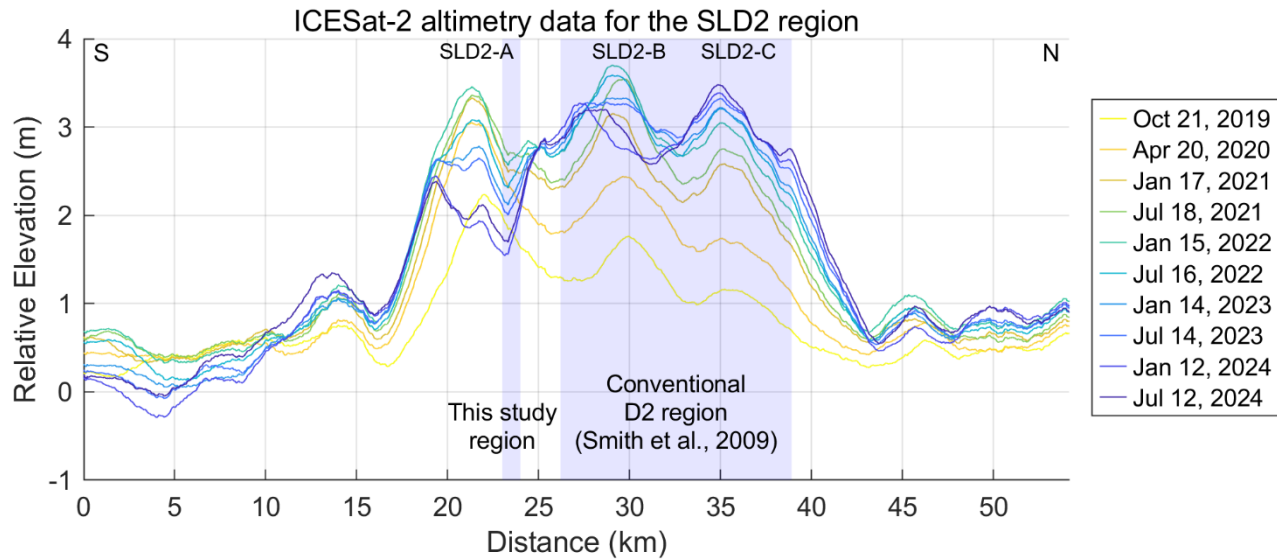
101
102 **Figure 1: Locations of subglacial lakes D1–D6 in the David Glacier region, Victoria Land, Antarctica (EPSG: 4326–WGS84).**
103

104 **2.2 Subglacial Lake D2**

105 Among the six subglacial lakes (D1–D6) identified beneath David Glacier via satellite altimetry (Smith et al., 2009; Wright
106 and Siegert, 2012), SLD2 was observed to have experienced a drainage event between 2003 and 2008 on the basis of ICESat
107 altimetry data (Smith et al., 2009). Since the drainage event, a continuous increase in surface elevation over SLD2 has been
108 observed, indicating water refilling, as detected from CryoSat-2 altimetry data (2013–2017) (Siegfried and Fricker, 2018) and,
109 more recently, from ICESat-2 observations (2019–2024) (Fig. 2). Figure 2 shows elevation changes relative to April 2019,

110 indicating surface uplift through January 2022. After this period, the surface elevation remained stable in the region originally
111 delineated as SLD2 by Smith et al. (2009), whereas a decreasing elevation trend was observed in the SLD2-A region (Ju et al.,
112 2025). These patterns of elevation change strongly suggest that SLD2 is an active subglacial lake, and that such drainage and
113 refilling are likely contributing to the presence of subglacial sediments (Siegfried et al., 2023).

114



115

116 **Figure 2: Glacier surface elevation changes derived from ICESat-2 altimetry between 22 April 2019 and 12 July 2024. The X-axis**
117 **corresponds to the 22 April 2019 dataset, and all subsequent elevation changes are referenced to this date. The light blue shaded**
118 **region indicates the spatial overlap between the conventional SLD2 region identified by Smith et al. (2009) and our study region.**

119

120 To better constrain the extent and basal conditions of SLD2, we used airborne IPR data collected during the 2016/17 (Lindzey
121 et al., 2020) and 2018/19 (Ju et al., 2025) field campaigns. These surveys show that the glacier surface elevations in the SLD2
122 region range from approximately 1820 to 1940 m. The corresponding ice thicknesses vary between 1685 and 2293 m.
123 Furthermore, the observations of moderately enhanced radar bed echoes relative to the surrounding area, elevated specularity
124 values (>0.4), depressed basal elevations (≤-350 m), the presence of a basin-like topography, a lower hydraulic head than the
125 surroundings, and low hydraulic gradients ($\leq 0.84^\circ$) collectively suggest a high potential for the presence of subglacial water
126 beneath SLD2. (Ju et al., 2025; Lindzey et al., 2020).

127 **3 Method**128 **3.1 Seismic survey**

129 As previously noted, the internal structure and water column of subglacial lakes cannot be fully resolved using IPR alone
 130 because of signal attenuation in water. Accordingly, a seismic survey was conducted within the candidate SLD2-A region
 131 identified from IPR data to investigate the structure of the subglacial lake more precisely.

132 During the 2019/20 austral summer, a preliminary seismic survey was conducted over the SLD2-A region to evaluate the
 133 potential presence of a subglacial lake and to obtain initial information on its structural characteristics. Owing to limited field
 134 time and equipment constraints, the fold of coverage for all survey lines was restricted to 1, and all shot points happened to be
 135 aligned near surface crevasses. Consequently, the acquired seismic data were significantly degraded by strong linear coherent
 136 noise generated by crevasses, severely compromising the quality of key reflectors, particularly those at the subglacial lake–
 137 bedrock interface. Furthermore, explosives were deployed in shallow boreholes (< 20 m depth), and due to the absence of
 138 proper backfilling, poor coupling between the explosives and the borehole walls further reduced energy transmission efficiency,
 139 resulting in overall low-quality reflection signals (Ju et al., 2024). Combined with the limitations of single-fold acquisition,
 140 stacking was not feasible, the dataset exhibited a low signal-to-noise ratio (SNR) and was unsuitable for quantitative structural
 141 interpretation. Nevertheless, the preliminary survey qualitatively confirmed the glacier thickness beneath SLD2-A and
 142 suggested the presence of subglacial water, providing critical baseline information that guided the methodology and survey
 143 design of the subsequent detailed seismic campaign conducted during the 2021/22 season.

144 For the refined survey, seismic acquisition lines were planned using bed topography derived from the IPR and surface elevation
 145 data from satellite altimetry. A total of four seismic lines were acquired and designated 21X, 21Y, 21XX, and 21YY (Fig. 3).
 146 Lines 21X and 21XX, oriented approximately 60° relative to the ice flow direction, are situated at an average surface elevation
 147 of 1894 ± 13 m. Lines 21Y and 21YY, oriented approximately -30° in the ice flow direction, lie at an average elevation of
 148 1887 ± 16 m. All lines traverse regions of minimal topographic relief, with average surface slopes of approximately 0.5°,
 149 indicating a relatively flat and stable glacier surface. The lengths of the 21X/21XX and 21Y/21YY lines are approximately 5
 150 km and 3.5 km, respectively. Seismic acquisition for lines 21X and 21Y was conducted using 8-fold coverage to increase the
 151 resolution, whereas lines 21XX and 21YY were acquired with 4-fold coverage due to time constraints during the survey. The
 152 additional acquisition parameters are summarized in Table 1.

153

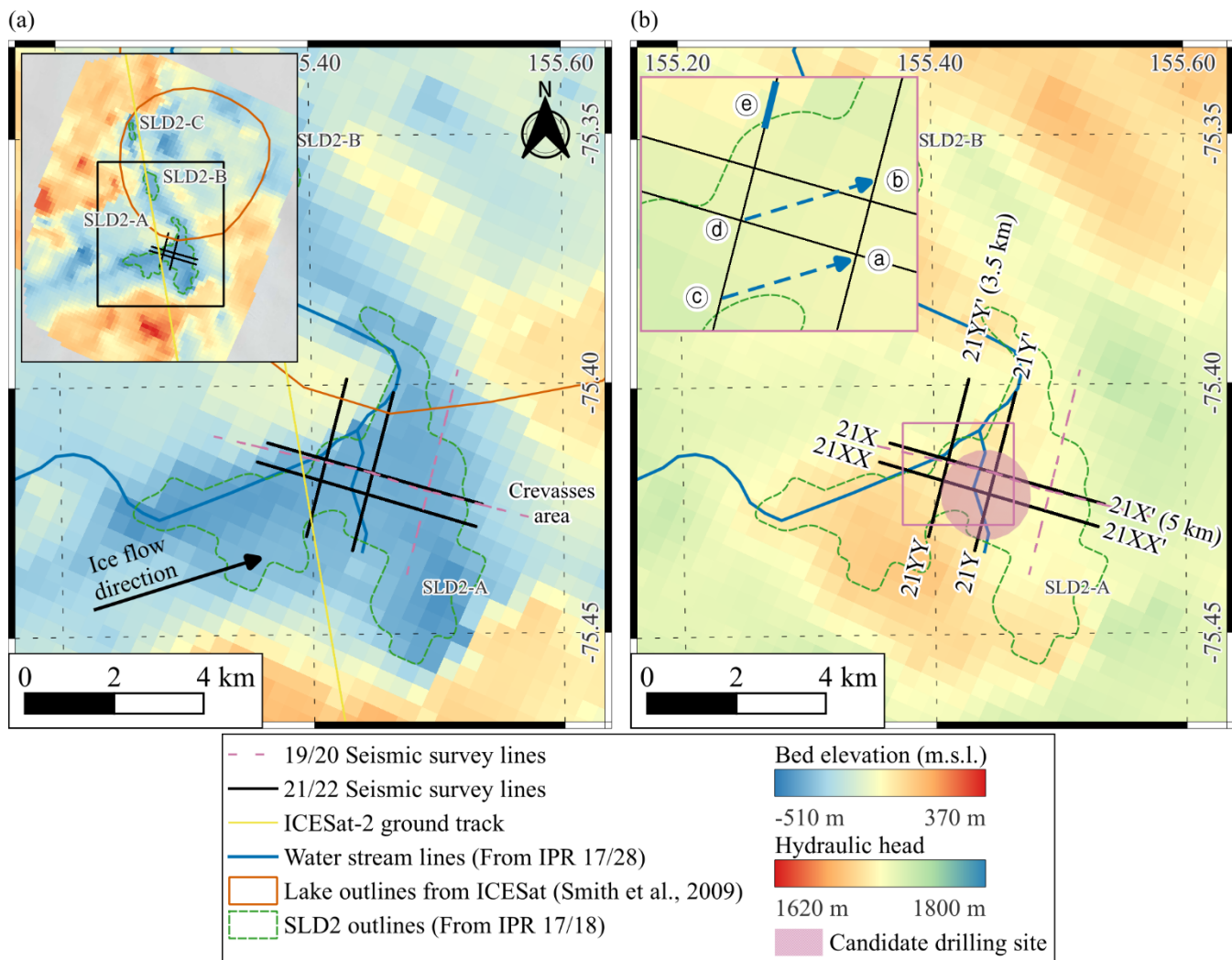
154 **Table 1: Parameters of the active-source seismic survey.**

Survey Parameters	Survey lines			
	21X line	21Y line	21XX line	21YY line
Line length (km)	5	3.5	5	3.5
Fold	8	8	4	4
Shot interval (m)	90	90	180	180
Number of shots	56	40	28	20

Shot positioning	Use both off-end and center shots
Receiver channels	96
Receiver interval (m)	15
Near offset (m)	0
Far offset (m)	1425
Recording time (s)	4
Record peak frequency (kHz)	1
Record sampling rate (ms)	0.25
Survey time (days)	34
Survey crew size	

Hot water drilling (3), Seismic (6)

155



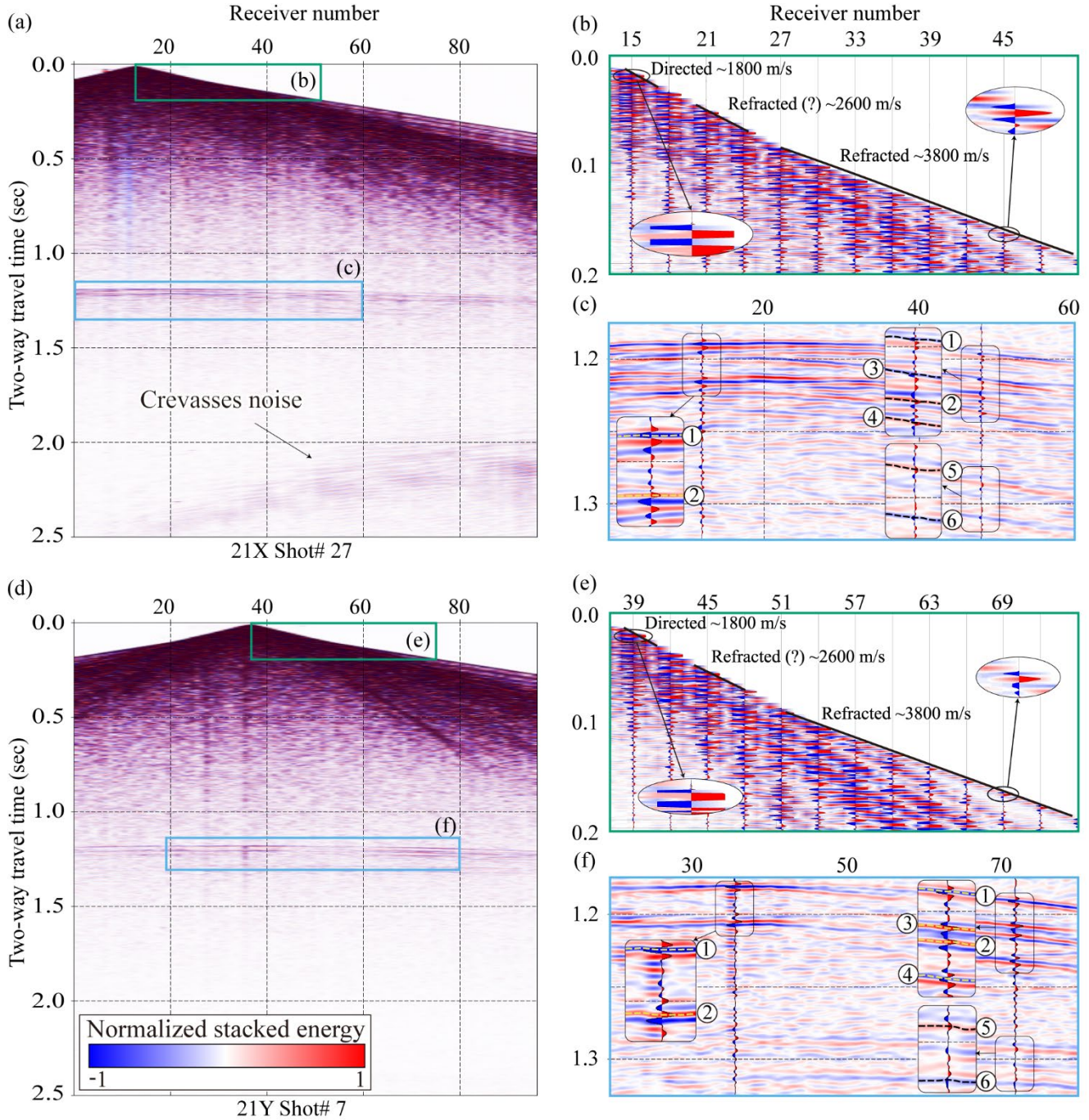
160 Before the seismic survey, a ground-penetrating radar (GPR) survey was used to identify the firn transition zone at depths of
161 approximately 20–22 m. To enhance seismic signal transmission, 1.6 kg of pentaerythritol tetranitrate (PETN) explosives were
162 emplaced at depths of 25–30 m using hot water drilling techniques. A total of 144 shots were deployed across the four survey
163 lines. Detailed shot positioning information is provided in the supplementary information S1. Given the snow-covered glacier
164 surface, Georods were used instead of conventional spike-type geophones to increase signal detection efficiency (Voigt et al.,
165 2013). Each Georod houses four geophone elements in a 0.6 m-long cylindrical array, producing a single output by summing
166 the inputs from all the elements. Compared with traditional geophones, this configuration improves coupling and detection
167 performance in snow-dominated environments (Voigt et al., 2013). Figure 4 presents shot gather #27 from line 21X and shot
168 gather #7 from line 21Y. In these shot gathers, both the direct wave and the refracted wave velocities were derived from first-
169 arrival travel-time analysis. The direct wave velocity was estimated to be approximately 1800 m s^{-1} , while the higher-velocity
170 arrival—interpreted as a refracted wave traveling through the firn–ice transition zone—exhibited an apparent velocity of
171 approximately 3800 m s^{-1} . First-arrival analysis of the direct wave indicates a normal polarity, confirming the source waveform
172 polarity. A prominent negative polarity reflection is observed at a two-way travel time (TWT) of approximately 1.2 s,
173 interpreted as the glacier–lake interface (①; See Table 2 for symbols definitions). Approximately 25–30 ms later, a ghost
174 reflection (②) with normal polarity appears. A subsequent reflection at approximately 1.3 s TWT, showing normal polarity,
175 is attributed to the bed interface (⑤), followed by its negative polarity ghost reflection (⑥) 25–30 ms later. In some shot
176 gathers, reflection signal (③) and its corresponding ghost signal (⑤) are observed. Notably, while signal ③ generally
177 appears with normal polarity in most records, it appears with reverse polarity in a few cases, such as Shot #27 on line 21X.
178 The survey was designed to place the seismic source at a distance from crevasses, ensuring that crevasse-related noise would
179 be recorded after the main reflections (1.1–1.3 s), thereby minimizing its impact (Figure 4a). While most data exhibit crevasse
180 noise occurring after the main reflections, a reduction in the source–crevasse distance causes this noise to increasingly overlap
181 with the primary arrivals, thereby complicating interpretation.

182

183 **Table 2: Symbols for each reflection event**

Interface symbols	Model 1	Model 2
①	Ice-water	Ice-water
②	Ice-water ghost	Ice-water ghost
③	-	Water-sediment
④	-	Water-sediment ghost
⑤	Water-bed	Sediment-bed
⑥	Water-bed ghost	Sediment-bed ghost
⑦	Ice-bed	Ice-sediment
⑧	Ice-bed ghost	Ice-sediment ghost

184



185

186 **Figure 4: Raw shot records from seismic lines 21X (a) and 21Y (d). Panels (b) and (e) are zoomed-in views of the early arrival window**
 187 **(0.0–0.2 s) from panels (a) and (d), respectively, used to calculate the apparent velocities of the direct and refracted waves. These**
 188 **panels highlight that the first arrivals of both the direct wave (clipped for display) and the refracted wave exhibit positive polarity.**
 189 **The direct wave, propagating through the upper firn layer (0–25 m depth), shows an apparent velocity of approximately 1800 m s⁻¹,**
 190 **while the refracted wave in firn–ice transition has an apparent velocity of approximately 3800 m s⁻¹. Panels (c) and (f) are zoomed-**

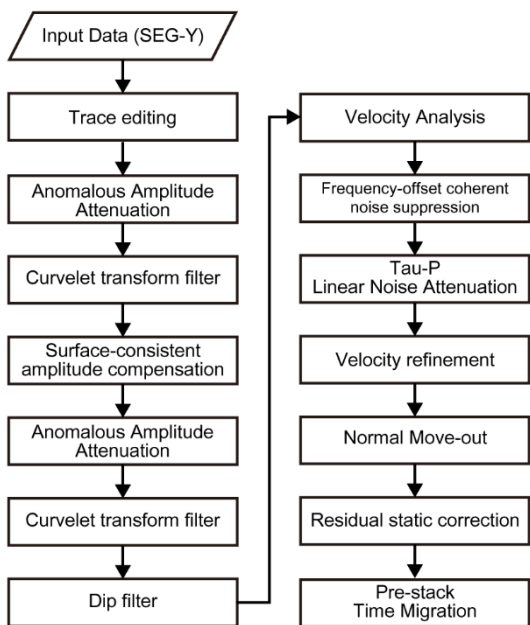
191 in views of the deeper arrivals (1.1–1.4 s) from panels (a) and (d), respectively. Reflections from the ice–water (①) interface exhibit
192 negative polarity, whereas those from the water/sediment–bed (⑤) interface display positive polarity.

193

194 **3.2 Seismic data processing**

195 Although seismic data acquired from glaciers share processing similarities with those of land-based surveys, glaciological
196 factors, such as surface cracks, crevasses, and strong winds, introduce substantial noise that can degrade data quality (Johansen
197 et al., 2011; Zechmann et al., 2018). Among these factors, linear noise generated by crevasses is particularly detrimental, often
198 obscuring key reflections (Dow et al., 2013). Hence, the glacier seismic data underwent multiple data processing sequences
199 focused on linear noise removal (Fig. 5). Acquisition geometry was added to the data using the raw data and geometry
200 information. Multiple data processing and noise removal processes were then carried out to increase the signal-to-noise ratio
201 (SNR).

202



203
204 **Figure 5: Schematic of the seismic data processing workflow based on the Omega geophysical data processing platform (SLB),**
205 **including noise attenuation, amplitude correction, velocity analysis, and prestack time migration.**

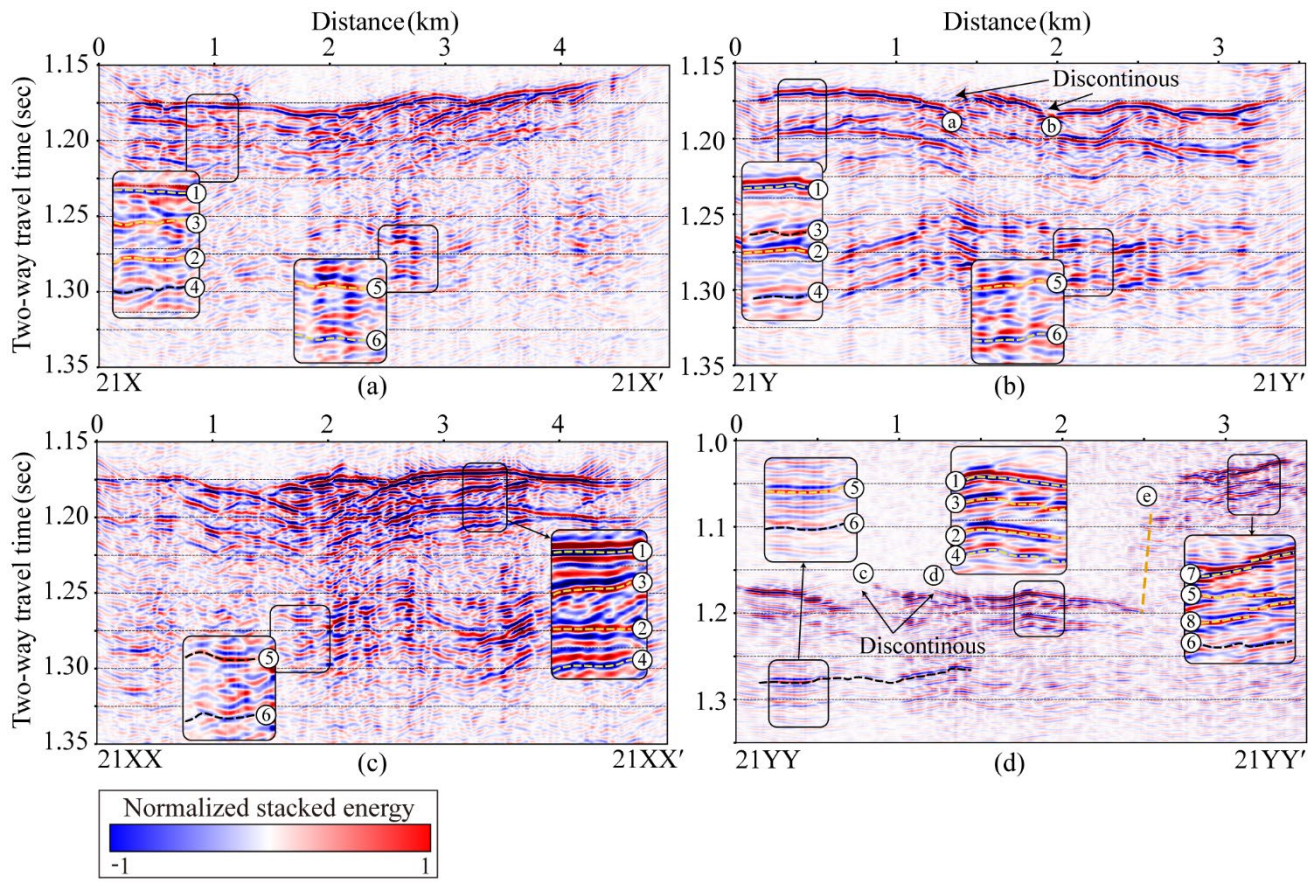
206

207 The initial processing involved anomalous amplitude attenuation (AAA), implemented via a spatial median filter. This step
208 targets outlier amplitudes within a defined frequency band, attenuating anomalous signals through interpolation across
209 neighboring traces. A curvelet transform-based filter was subsequently applied to remove coherent noise. Curvelet
210 decomposition enables the separation of signals on the basis of dip angle and scale, allowing for the selective removal of

211 ground roll and other coherent noise components that differ in dip from true reflections (Oliveira et al., 2012). In this study,
212 linear coherent noise at later arrival times (>2.0 s) was effectively removed using this method.
213 Surface-consistent amplitude compensation (SCAR) and surface-consistent deconvolution were employed to normalize the
214 amplitude variability across shot gathers. These steps were followed by a second round of AAA and curvelet filtering to
215 suppress artifacts introduced during the compensation and deconvolution stages. Dip filtering was also applied to eliminate
216 spurious hyperbolic arrivals, which were manually identified and removed.
217 Velocity analysis was conducted at intervals of 40 common midpoints to construct a migration velocity model. Frequency–
218 offset coherent noise suppression (FXCNS) was used to attenuate linear-related noise, followed by Tau-p linear noise
219 attenuation (LNA), effectively reducing the noise associated with crevasse scattering. The final processing steps included
220 velocity model refinement, normal move-out (NMO) correction, and prestack time migration (PSTM). The specific parameters
221 employed for data processing, as well as the intermediate outcomes at each processing stage, are provided in the supplementary
222 information S2.
223 To increase imaging accuracy, a residual static correction was applied before migration using glacier surface elevation data.
224 The final migrated seismic section was produced using Kirchhoff PSTM. The migrated data have a center frequency of
225 approximately 180 Hz. Assuming seismic wave velocities between 1396 m s^{-1} (water) and 3800 m s^{-1} (ice), the corresponding
226 vertical resolutions, which are calculated using the quarter-wavelength criterion, range from approximately 2.0 m to 5.3 m.
227 The data can image both the top and bottom of a water column approximately 2 m thick or thicker.

228 **4 Seismic data processing results**

229 Figure 6 presents the PSTM results for the four seismic survey lines. On line 21X (Fig. 6a), a strong, laterally continuous
230 reflection with reverse polarity is observed at 0.3–4.8 km along the profile, and the two-way travel time (TWT) is
231 approximately 1.15–1.18 s. This reflection is interpreted as the glacier–lake interface (①). Approximately 25–30 ms below
232 this horizon, a normal polarity reflection (②) appears, likely representing a ghost signal associated with the primary glacier–
233 lake reflection. Between reflections ① and ②, a weak normal polarity reflection (③), presumed to represent an interface, is
234 observed. However, in some shot gathers, signal ③ appears with reverse polarity (Figure 4c), leading to partial cancellation
235 and ambiguity in layer interpretation. Approximately 25 ms later, an opposite polarity ghost reflection (④) follows. A deeper
236 normal polarity reflection is observed within 1.9–3.1 km at TWTs of 1.25–1.27 s (⑤), which is interpreted as the bed interface.
237 This is followed by a reverse polarity reflection 25–30 ms later (⑥), which is presumed to be the corresponding ghost of the
238 bed interface.



239
 240 **Figure 6: PSTM seismic sections for lines (a) 21X, (b) 21Y, (c) 21XX, and (d) 21YY prior to ghost removal. Ghost reflections appear**
 241 **25–30 ms beneath the glacier–lake and lake–bed interfaces due to the 25 m source depth. See Table 2 for symbols definitions.**

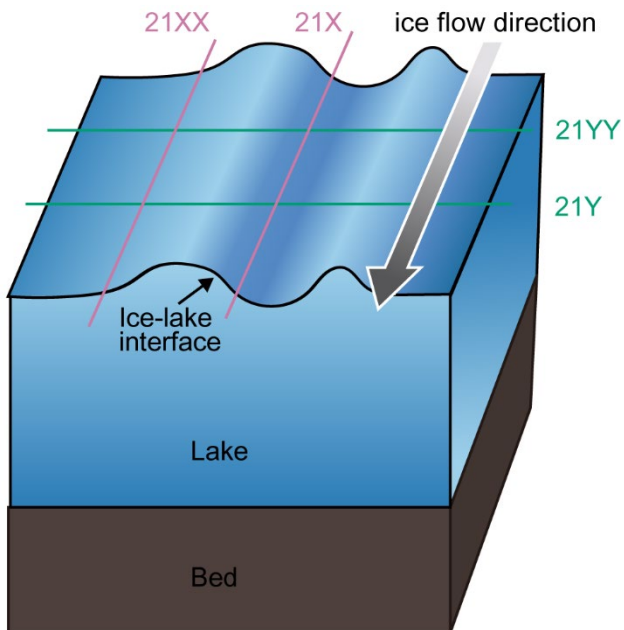
242
 243 In line 21Y (Fig. 6b), similar features are observed. A reverse polarity reflection, interpreted as the glacier–lake interface (①),
 244 is observed within 0.1–3.2 km at TWT 1.17–1.18 s, with its ghost reflection (②), which exhibits normal polarity and appears
 245 25–30 ms later. Between reflections ① and ②, a weak normal polarity reflection (③), presumed to represent an interface, is
 246 observed in some areas, followed approximately 25 ms later by an opposite polarity ghost reflection (④). A normal polarity
 247 reflection within 0.1–3.2 km at a TWT of 1.26–1.27 s is interpreted as the bed interface (⑤), followed by a reverse polarity
 248 ghost signal (⑥). Additionally, discontinuous reflections interpreted as subglacial scour-like features (SLF) are visible at
 249 approximately 1.3 km (ⓐ) and 1.9 km (ⓑ) along line 21Y at TWT 1.18 s (black arrows in Fig. 6b). These features may be
 250 associated with glacial erosion of the underlying substrate.
 251 In line 21XX (Fig. 6c), a reverse polarity reflection, interpreted as the glacier–lake interface (①), is observed within 0–4.3
 252 km at a TWT of 1.17–1.18 s. This reflection is followed 25–30 ms later by a normal polarity reflection (②), which is
 253 considered the ghost of the primary glacier–lake interface. Between reflections ① and ②, a weak normal polarity reflection

254 (③), presumed to represent an interface, is observed in some areas, followed approximately 25 ms later by an opposite polarity
255 ghost reflection (④). Further down the section, a normal polarity reflection (⑤) within 1.9–4.2 km at a TWT of 1.25–1.28 s
256 is interpreted as the bed interface, followed by its ghost reflection (⑥) 25–30 ms later.

257 On line 21YY (Fig. 6d), the glacier–lake interface (①) is marked by a strong, flat, reverse polarity reflection at 0–2.4 km and
258 a TWT of 1.17–1.20 s, followed by its normal polarity ghost (②) 25–30 ms below. A weak normal polarity reflection (③),
259 presumed to represent an interface, is observed between ① and ②, followed approximately 25 ms later by a opposite polarity
260 ghost reflection (④). Bed interface reflections (⑤) are observed within 0.2–2.4 km at TWTs of 1.27–1.29 s, followed by a
261 reverse polarity ghost (⑥) 25–30 ms later. Within 2.4–2.55 km and TWTs of 1.08–1.17 s, no coherent reflection is visible
262 due to the steeply dipping bed topography, as indicated by the dashed orange (⑧) line in Fig. 6d. Within 2.55–3.4 km and a
263 TWT of 1.03–1.09 s, a reverse polarity reflection (⑦), likely originating from a mildly dipping sedimentary surface, is
264 observed, followed by an opposite polarity ghost reflection (⑧). Additionally, although weak, reflection signal (⑤) and its
265 corresponding ghost (⑥) are also identified. Additionally, similar to observations on line 21Y, discontinuous reflections
266 interpreted as SLF surfaces appear at 0.7 km (⑨) and 1.2 km (⑩) along line 21YY at TWT 1.18 s (black arrows in Fig. 6d).

267 The discontinuous reflection signals identified on lines 21Y and 21YY are spatially aligned along the ice flow direction when
268 projected laterally (Fig. 3, dashed blue arrow). This alignment suggests that the observed discontinuities correspond to a
269 subglacial SLF surface formed by glacial motion. The SLF is visible predominantly on lines 21Y and 21YY, which are oriented
270 more perpendicularly to the ice flow direction, thereby enhancing the expression of lateral subglacial variability. In contrast,
271 lines 21X and 21XX are more parallel to the ice flow, resulting in a foreshortened view of the subglacial structures and a
272 relatively flat appearance in the seismic sections (Fig. 7).

273



274

275 **Figure 7: Conceptual diagram illustrating the orientation of seismic survey lines relative to subglacial structures and the ice flow**
 276 **direction, explaining the appearance of structural features in each line.**

277

278 **5 Comparison between field data and synthetic seismograms**

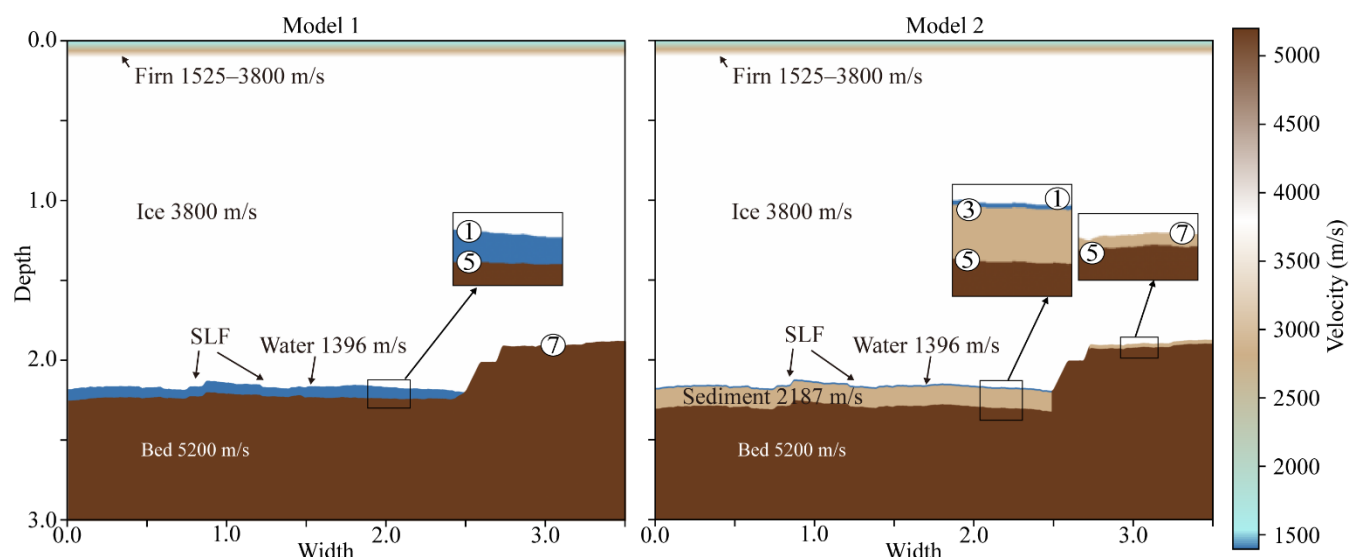
279 In all seismic profiles, the glacier–water interface (①) is characterized by strong, reverse polarity reflections. Following this,
 280 a relatively weaker reflection (③) with limited lateral continuity, which may indicate an unconsolidated sediment layer, or an
 281 unknown interface beyond the scope of current interpretation.

282 Interpreting field seismic data presents inherent challenges due to limited subsurface information, high levels of ambient noise,
 283 and signal attenuation. These issues are particularly pronounced at the SLD2 site, where the absence of borehole data
 284 introduces significant uncertainty and potential inaccuracies in depth estimations derived from PSTM sections. Such
 285 limitations may lead to misinterpretations of stratigraphic boundaries (Herron, 2000; Yilmaz, 2001). To address these
 286 challenges, this study developed a subsurface structural model and conducted a comparative analysis of synthetic seismograms
 287 generated from the model with observed field data. Focusing on the interpretation of basal reflections beneath the subglacial
 288 lake—excluding the glacier–lake interface (①)—two plausible structural models were proposed. Model 1 assumes the absence
 289 of a sedimentary layer, in which reflection (③) is not present, and reflection (⑤) represents the base of the subglacial lake.
 290 In contrast, Model 2 includes a sedimentary layer, where reflection (③) corresponds to the lake–sediment interface and
 291 reflection (⑤) indicates the sediment–bedrock interface (Figure 8). The synthetic data were generated using a time-domain
 292 forward modeling approach based on the staggered grid finite difference method (Graves et al., 1996). The velocity model

used in the simulation was constructed based on field velocity analysis and previously published data, and included stratigraphic units representing firn, glacial ice, subglacial water, sediment, and bedrock. Each layer was assigned appropriate P-wave velocities and density values. P-wave velocities in firn vary from 1525 to 3800 m s⁻¹ because density increases with depth (Kirchner and Bentley, 1979; Picotti et al., 2015; Qin et al., 2024). Glacial ice has an average P-wave velocity of approximately 3800 ± 5 m s⁻¹ at -2 ± 2 °C (Kohnen, 1974), while subglacial water has a velocity of approximately 1396 ± 2 m s⁻¹ at -1.75 ± 0.25 °C, with a salinity less than 1 PSU (practical salinity units) (Thoma et al., 2010; Tulaczyk et al., 2014). The P-wave velocities of the sediment and bed were referenced from the Lake Vostok model value (Carcione & Gei, 2003). Forward modeling was then conducted using the Ricker wavelet, with acquisition parameters matching those used in the field survey (Table 3). We applied just the migration step in case of the synthetic dataset, as it is free of noise.

303 **Table 3: Parameters of the synthetic model.**

Synthetic modeling parameters																											
Model size	3.5 km (distance) x 3 km (depth)																										
Source	Ricker wavelet (zero-phase), 60 Hz																										
Receiver	25 m depth, 90-m interval																										
Grid spacing	0 m depth, 15-m interval, 96 channel																										
Sampling interval	0.5-m																										
Layer parameters	<table> <thead> <tr> <th></th><th>Thickness (m)</th><th>Velocity (m s⁻¹)</th><th>Density (g cm⁻³)</th></tr> </thead> <tbody> <tr> <td>Firm</td><td>100</td><td>1525–3800</td><td>0.3–0.917</td></tr> <tr> <td>Ice</td><td>1887–2221</td><td>3800</td><td>0.917</td></tr> <tr> <td>Water (Model 1, 2)</td><td>53–82 / 10</td><td>1396</td><td>1.017</td></tr> <tr> <td>Sediment (Model 2)</td><td>120</td><td>2817</td><td>2.128</td></tr> <tr> <td>Bed</td><td></td><td>5200</td><td>3.2</td></tr> </tbody> </table>				Thickness (m)	Velocity (m s ⁻¹)	Density (g cm ⁻³)	Firm	100	1525–3800	0.3–0.917	Ice	1887–2221	3800	0.917	Water (Model 1, 2)	53–82 / 10	1396	1.017	Sediment (Model 2)	120	2817	2.128	Bed		5200	3.2
	Thickness (m)	Velocity (m s ⁻¹)	Density (g cm ⁻³)																								
Firm	100	1525–3800	0.3–0.917																								
Ice	1887–2221	3800	0.917																								
Water (Model 1, 2)	53–82 / 10	1396	1.017																								
Sediment (Model 2)	120	2817	2.128																								
Bed		5200	3.2																								



306 **Figure 8: P-wave velocity model used in forward modeling for line 21YY. The upper ~100 m represents firn with velocities ranging**
307 **from 1525–3800 m s⁻¹ (Kirchner and Bentley, 1979; Picotti et al., 2015; Qin et al., 2024). The ice below this depth has a velocity of**
308 **3800 ± 5 m s⁻¹ (Kohnen, 1974), and the subglacial water layer has a velocity of 1396 ± 2 m s⁻¹ (Thoma et al., 2010; Tulaczyk et al.,**
309 **2014). In Model 2, the velocity of 2817 m s⁻¹ for the sediment layer was taken from the lower sediment layer model of Lake Vostock**
310 **(Carcione & Gei, 2003).**

311

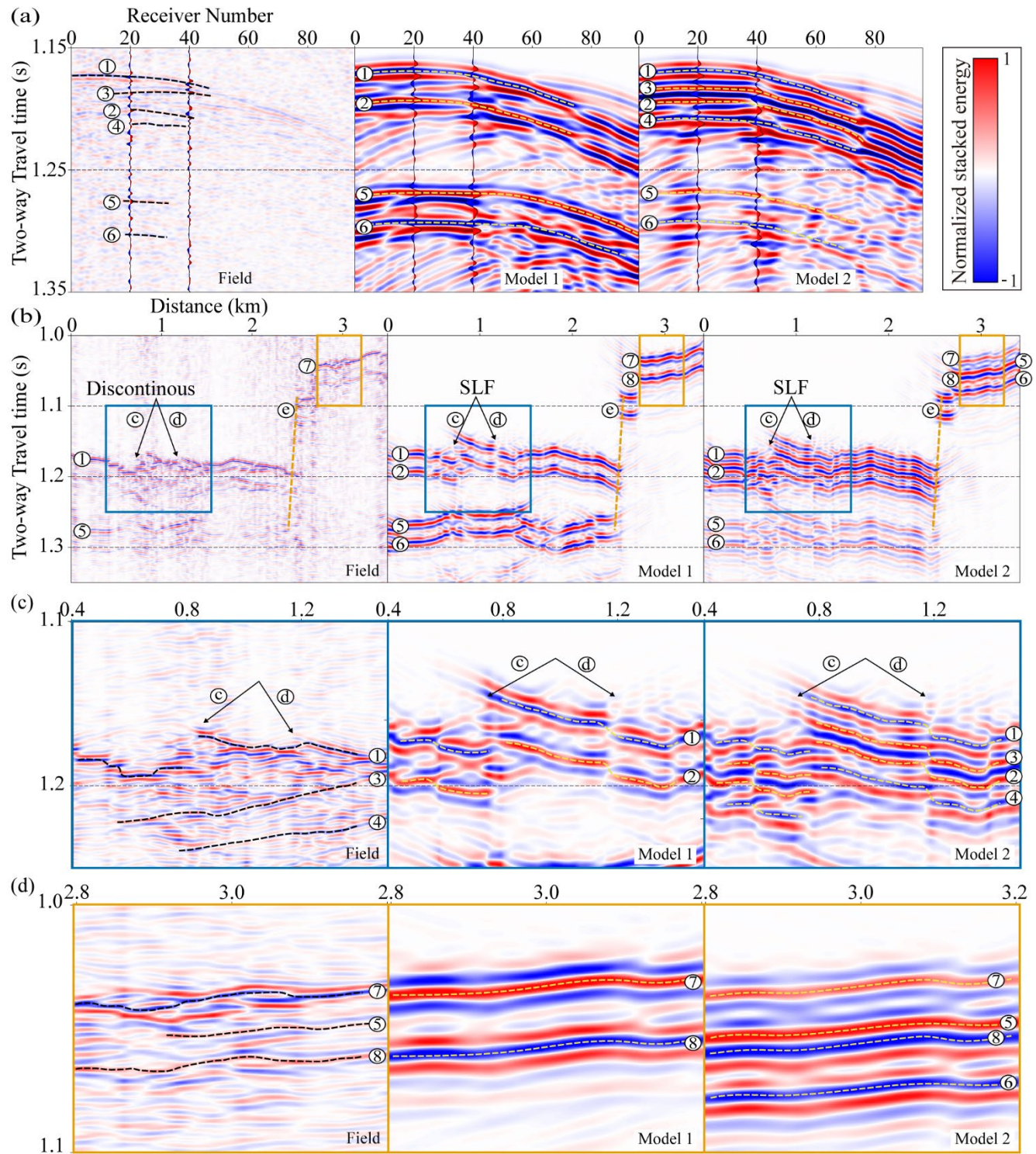
312 Figure 9a compares the shot gather from seismic data line 21YY (left) with those from the synthetic datasets for Models 1 and
313 2 (center, right). A prominent reflection at a TWT of 1.17 s is observed in both datasets, corresponding to the glacier–lake
314 interface (①). This reflection results in a high impedance contrast and reverse polarity due to the P-wave velocity difference
315 between glacial ice and water. These features are consistent with previous observations at glacier–lake interfaces (Atre and
316 Bentley, 1993; Brisbourne et al., 2023; Horgan et al., 2012; King et al., 2004; Peters et al., 2007; Woodward et al., 2010). A
317 secondary reflection with normal polarity appears approximately 28 ms after the primary event (②) and is interpreted as a
318 surface ghost reflection. This time delay corresponds to a seismic source depth of approximately 25 m, which is consistent
319 with previous seismic analyses (Brisbourne et al., 2023; Schlegel et al., 2024). That is, assuming an average P-wave velocity
320 of 1800 m s⁻¹ within the top 25 m, the TWT of the ghost reflection matches the expected delay:

321
$$\text{TWT}_{\text{ghost}} = \frac{2 \times 25 \text{ m}}{1800 \text{ m s}^{-1}} \approx 28 \text{ ms.} \quad (1)$$

322 Furthermore, considering that the acoustic impedance of air is approximately zero ($Z_{\text{air}} \approx 0$) and that of ice is Z_{ice} , the
323 reflection coefficient (RC) for an upgoing wave at the air–ice interface can be approximated as follows:

324
$$RC = \frac{Z_{\text{air}} - Z_{\text{ice}}}{Z_{\text{ice}} + Z_{\text{air}}} \approx -1. \quad (2)$$

325 This implies that the polarity of the ghost reflection at the surface is reversed relative to the downgoing primary wave (Kralil
326 and Shin, 1990; Robinson and Treitel, 2008).



327

328 **Figure 9: Comparison of field seismic data and synthetic results from Model 1 and 2. (a) Shot gathers at the same location from the**
 329 **21YY field data (left) and synthetic models (center: Model 1, right: Model 2). (b) Comparison of PSTM images from the 21YY line**

330 and the two synthetic models. (c) Enlarged views of discontinuous reflections. (d) Comparison of dipping bed reflections, showing
331 shadow zones and steep basal topography.

332

333 Figure 9b compares the PSTM sections of the field data from line 21YY and the two synthetic models. Unlike the field data,
334 the synthetic dataset is free from ambient noise and features a precise source–receiver geometry, resulting in clearer delineation
335 of subsurface reflections and facilitating structural interpretation. In the PSTM sections of both the synthetic models (Model 1
336 and Model 2) and the field data, three primary reflection events (①, ⑤, ⑦) and their corresponding source-generated ghost
337 reflections (②, ⑥, ⑧) are observed at similar two-way travel times. Reflections ①, ②, ⑤, and ⑥ also exhibit consistent
338 polarity across the synthetic and field datasets. Additionally, the lateral discontinuities in reflections generated by the SLF
339 structure implemented in the velocity model closely resemble those observed in the field data. The orange dashed line (⑩)
340 delineates the shape of the bedrock forming the margin of the subglacial lake, interpreted to dip at approximately 52°.

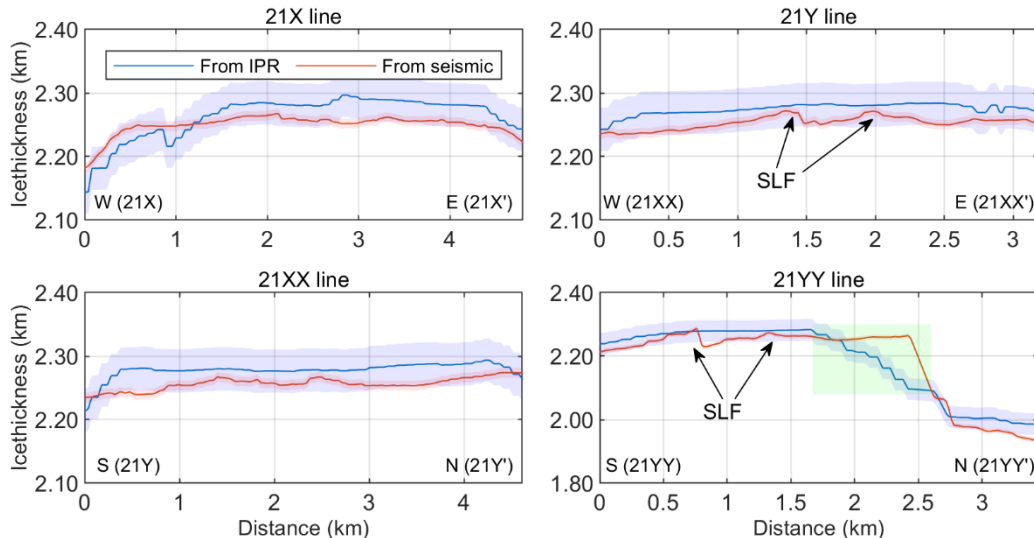
341 Figure 9c presents an enlarged comparison between the field and synthetic PSTM sections, focusing on the region of lateral
342 reflection discontinuities. In the field data, discontinuous reflections and associated low reflectivity observed at approximately
343 0.7 km and 1.2 km (TWT = 1.18 s) complicate interpretation. To simulate this feature, the velocity model incorporates a
344 concave structure at the beneath the glacier, representing the SLF. The resulting reflection patterns in the synthetic section
345 closely resemble those observed in the field data. In the field data, the reflection from the water–sediment interface (③) is
346 weak and poorly defined, resulting in significant interpretational uncertainty. This is attributed in part to the diffusive interface
347 of the unconsolidated upper sediment, which weakens reflection strength. Moreover, the short temporal separation between
348 reflection ③ and the preceding ghost reflection (②) results in significant waveform interference, often producing a single,
349 high-amplitude composite signal. Overlap between reflections ② and ③ leads to destructive interference, further
350 complicating the identification of the interface. In some areas, the ghost reflection (④) is unaffected by such interference,
351 allowing for an indirect estimation of the ③ interface using ghost travel-time differences. However, due to the difficulty in
352 clearly resolving this interface throughout the dataset, Model 2 was constructed using a uniform geometry derived from the
353 average time interval between reflections ① and ③, corresponding to a water depth of 10 m and a sediment thickness of 120
354 m. As a result, the arrival time and waveform characteristics of reflection ③ in the synthetic data exhibit slight discrepancies
355 when compared to those observed in the field data.

356 Figure 9d presents a magnified comparison of regions synthetic and field to examine reflections from a dipping bed. Within
357 2.4–2.55 km and TWTS of 1.08–1.17 s, reflections are temporally dispersed, resulting in a shadow zone where coherent signals
358 are absent. A noteworthy feature is the polarity reversal of reflections ⑦ and ⑧ between the field and synthetic datasets. In
359 the velocity models, the ⑦ interface is defined as either the glacier–bedrock interface in Model 1 or the glacier–sediment
360 interface in Model 2. In Model 1, the bedrock has significantly higher acoustic impedance than the overlying ice, due to its
361 greater density and seismic velocity, resulting in a high amplitude reflection with normal polarity. Conversely, the sediment
362 layer in Model 2 is assigned a lower seismic velocity but higher density relative to glacial ice, yielding a slightly higher
363 impedance and thus a reflection of lower amplitude. However, the field data show that reflection ⑦ exhibits reversed polarity,

364 suggesting the presence of subglacial sediments with lower acoustic impedance than assumed in the models. This discrepancy
365 may be explained by the presence of a dilatant till beneath the glacier, which can produce reverse polarity reflections depending
366 on its physical properties. Booth et al. (2012) demonstrated that the seismic response of such tills is highly sensitive to
367 variations in P-wave velocity, density, and thickness. In particular, their study showed that when the till forms a thin layer,
368 reverse polarity reflections may occur. While the existence of such glacial sediments presents a plausible interpretation for the
369 study area, the absence of reliable constraints on their seismic properties precluded their incorporation into the velocity models
370 used in this study.

371 To further validate the interpretation, ice thickness estimates from the seismic data were compared with those derived from
372 airborne IPR surveys (Ju et al., 2025) along four seismic lines (Fig. 10). Given the lack of spatial coincidence between seismic
373 and IPR profiles, kriging-based two-dimensional interpolation (Isaaks and Srivastava, 1989) was applied to the IPR dataset to
374 estimate the ice thickness at seismic line locations. The uncertainties associated with the IPR and seismic datasets are ± 33.4 m
375 and ± 7.6 m, respectively at the 99% confidence level (Supplementary information S3). Consequently, the combined
376 uncertainty of both datasets is approximately ± 34 m. The root mean square error (RMSE) between the two datasets is calculated
377 as approximately ± 29 m. When excluding between 1.7 and 2.6 km along seismic line 21YY—within the light green shaded
378 area in Fig. 10—where significant interpolation-induced smoothing effects occur in the IPR data, the RMSE is reduced to
379 approximately ± 25 m. This result indicates a high degree of consistency between the seismic and IPR datasets. The ice
380 thickness derived from radar data is generally greater than that obtained from seismic data across most areas. This discrepancy
381 may be attributed to an overestimation of the radar velocity. Ju et al. (2025) adopted a commonly used literature-based radar
382 velocity of 0.169 m ns^{-1} , which may differ from the actual radar velocity in the study area. Additionally, the uncertainty in
383 measuring the ice bottom in the radar data is ± 32.7 m, and this must be considered when comparing the two datasets. Despite
384 these factors, the two datasets show a high level of consistency within the uncertainty bounds. This consistency supports the
385 mutual reliability of both methods and validates their integrated application for subglacial lake characterization.

386 As additional supporting evidence for this interpretation, a steeply dipping (©) bedrock interface observed along the 21YY
387 line is consistently identified in both the seismic PSTM profile (Figure 9d) and the IPR-derived ice thickness graph (Figure
388 10), indicating a similar topographic transition in both datasets. This interface is interpreted as a structural margin delineating
389 the lateral extent of SLD2 and likely functions as a hydrological barrier. The structural congruence observed in both seismic
390 and radar data underscores the effectiveness of integrating these datasets to delineate the boundaries of subglacial lakes,
391 particularly in regions characterized by complex basal topography.



392

393 **Figure 10:** A comparison of ice thickness estimates derived from seismic and kriging-interpolated IPR data (Ju et al., 2025) along
 394 the four seismic survey lines reveals high overall consistency between the two datasets, despite localized discrepancies. The light
 395 green shaded region in the 21YY line represents areas where interpolation contributes to the divergence between the two
 396 measurement approaches. The light blue envelope represents the uncertainty bounds associated with the IPR-derived estimates,
 397 while the light red envelope indicates uncertainty bounds for the seismic-derived estimates.

398 6 Conclusion

399 Since 2016, the Korea Polar Research Institute (KOPRI) has conducted a series of geophysical investigations to study SLD2
 400 (Subglacial Lake Cheongsuk) beneath David Glacier, beginning with airborne IPR surveys. In 2021, a seismic survey was
 401 carried out to characterize the internal structure and water column of SLD2. The field seismic data revealed a strong, reverse
 402 polarity reflection at the glacier–lake interface. In contrast, the basal reflections beneath the lake are less well-defined,
 403 suggesting the presence of subglacial sediments. This ambiguity gives rise to two alternative interpretive scenarios based on
 404 the presence or absence of a sedimentary layer.

405 Given this interpretational ambiguity regarding the sediment layer, two velocity models were constructed: Model 1, which
 406 assumes the absence of sediment, and Model 2, which includes a sediment layer beneath the lake. Synthetic seismology was
 407 generated using wave propagation modeling based on these models. Sediment thickness in Model 2 was uniformly assigned
 408 using the average time difference calculated from selected areas of the dataset. Comparisons between the synthetic and field
 409 PSTM sections show consistent TWT times and polarities for key reflection events at the glacier–lake interface, the lake–
 410 bedrock interface in Model 1, and the sediment–bedrock interface in Model 2. Nevertheless, synthetic data generated by
 411 modeling a velocity model that simplifies a complex geological structure has limitations in thoroughly explaining the entire
 412 waveform of the complex field data. For example, subglacial sediments are generally expected to produce normal polarity
 413 reflections due to acoustic impedance contrasts with overlying water. However, in field data, the polarity and clarity of the

414 water-sediment interface vary with the degree of sediment consolidation. In particular, the reverse polarity reflection observed
415 at the ice–sediment interface in the 21YY profile suggests the potential presence of dilatant till.
416 This study demonstrates the utility of seismic surveying for analyzing structural characteristics of subglacial lake environments
417 that are not identified with conventional radar. Furthermore, the integrated analysis of seismic and synthetic data provides a
418 quantitative structural model of the SLD2-A geometry beneath David Glacier. These results provide critical guidance for future
419 clean hot-water drilling. In particular, we identify an area within a 1 km radius of S 75.422°, E 155.441° as a suitable candidate
420 site, based on its broad spatial extent, minimum estimated water depth exceeding approximately 10 m, and absence of
421 contamination from surface field camps. Furthermore, we plan to conduct follow-up studies incorporating advanced processing
422 techniques such as deghosting, amplitude variation with offset analysis, and the development of a refined velocity model that
423 accounts for detailed firn-layer properties. These technical advancements are expected to enhance the resolution and precision
424 of seismic imaging and contribute to a deeper understanding of the subglacial environment.

425 **Data availability**

426 The ICESat-2 data used in this study are available from the National Snow and Ice Data Center (NSIDC). The seismic data
427 and ICESat-2 laser altimetry data used in this study are also available from the Korea Polar Data Center (KPDC) upon request
428 at <https://dx.doi.org/doi:10.22663/KOPRI-KPDC-00001177>. The maps related to Antarctica were created using the
429 Quantarctica dataset version 3.2 (Matsuoka et al., 2018).

430 **Author contributions**

431 HJ: Writing—original draft, investigation, methodology, conceptualization. SGK: Writing—original draft, methodology,
432 conceptualization, supervision. YC: Writing – original draft, data processing, modeling. SP: Data processing methodology.
433 MJL: Writing – original draft. HK: Hot-water drilling. KK: Investigation. YK: Investigation. JIL: Project administration,
434 Funding acquisition.

435 **Competing interests**

436 The authors declare that they have no known competing financial interests or personal relationships that could have appeared
437 to influence the work reported in this paper.

438 **Acknowledgments**

439 We express our sincere gratitude to Sungjun Jeon and the K-route team for their invaluable logistical support. We also extend
440 our appreciation to Do-youn Kwon, Jamin Park, Sanghyeok Seo, and Byeongguk Moon for their dedicated assistance in

441 seismic surveys. We name Subglacial Lake D2 Subglacial Lake Cheongsuk (SLC). The name Cheongsuk has a significant
442 meaning, as it is the pen name of Dr. Yeadong Kim, the founder of the KOPRI and former president of the Scientific Committee
443 on Antarctic Research (SCAR). Dr. Kim personally led the IPR and seismic surveys of Subglacial Lake Cheongsuk and
444 coauthored this paper.

445

446 **Financial support**

447 This research was supported by KOPRI grants funded by the Ministry of Oceans and Fisheries (KOPRI project Nos. PE26080).
448

449 **References**

450 Atre, S. R. and Bentley, C. R.: Laterally varying basal conditions beneath ice Streams B and C, West Antarctica,
451 *J. Glaciol.*, 39, 507–514, <https://doi.org/10.3189/s0022143000016403>, 1993.

452 Bell, R. E., Studinger, M., Shuman, C. A., Fahnestock, M. A., and Joughin, I.: Large subglacial lakes in East
453 Antarctica at the onset of fast-flowing ice streams, *Nature*, 445, 904–907,
454 <https://doi.org/10.1038/nature05554>, 2007.

455 Bell, R. E., Ferraccioli, F., Creyts, T. T., Braaten, D., Corr, H., Das, I., Damaske, D., Frearson, N., Jordan, T.,
456 Rose, K., Studinger, M., and Wolovick, M.: Widespread persistent thickening of the east antarctic ice sheet
457 by freezing from the base, *Science*, 331, 1592–1595, <https://doi.org/10.1126/science.1200109>, 2011.

458 Bentley, M. J., Hodgson, D. A., Smith, J. A., Cofaigh, C. Ó., Domack, E. W., Larter, R. D., Roberts, S. J.,
459 Brachfeld, S., Leventer, A., Hjort, C., Hillenbrand, C. D., and Evans, J.: Mechanisms of Holocene
460 paleoenvironmental change in the Antarctic Peninsula region, *Holocene*, 19, 51–69,
461 <https://doi.org/10.1177/0959683608096603>, 2009.

462 Booth, A. D., Clark, R. A., Kulessa, B., Murray, T., Carter, J., Doyle, S., and Hubbard, A.: Thin-layer effects in
463 glaciological seismic amplitude-versus-angle (AVA) analysis: implications for characterising a subglacial till
464 unit, *Russell Glacier, West Greenland, Cryosphere*, 6, 909–922, <https://doi.org/10.5194/tc-6-909-2012>, 2012.

465 Brisbourne, A. M., Smith, A. M., Rivera, A., Zamora, R., Napoleoni, F., Uribe, J. A., and Ortega, M.:
466 Bathymetry and bed conditions of Lago Subglacial CECs, West Antarctica, *J. Glaciol.*, 69, 1–10,
467 <https://doi.org/10.1017/jog.2023.38>, 2023.

468 Carcione, J. M., and Gei, D.: Seismic modelling study of a subglacial lake. *Geophysical Prospecting*, 51(6), 501–
469 515. <https://doi.org/10.1046/j.1365-2478.2003.00388.x>, 2003.

470 Christianson, K., Jacobel, R. W., Horgan, H. J., Anandakrishnan, S., and Alley, R. B.: Subglacial Lake Whillans
471 — Ice-penetrating radar and GPS observations of a shallow active reservoir beneath a West Antarctic ice
472 stream, *Earth Planet. Sc. Lett.*, 331-332, 237–245, <https://doi.org/10.1016/j.epsl.2012.03.013>, 2012.

473 Christner, B. C., Priscu, J. C., Achberger, A. M., Barbante, C., Carter, S. P., Christianson, K., Michaud, A. B.,
474 Mikucki, J. A., Mitchell, A. C., Skidmore, M. L., Vick-Majors, T. J., Adkins, W. P., Anandakrishnan, S.,
475 Barcheck, G., Beem, L., Behar, A., Beitch, M., Bolsey, R., Branecky, C., Edwards, R., Fisher, A., Fricker, H.
476 A., Foley, N., Guthrie, B., Hodson, T., Horgan, H., Jacobel, R., Kelley, S., Mankoff, K. D., McBryan, E.,
477 Powell, R., Purcell, A., Sampson, D., Scherer, R., Sherue, J., Siegfried, M., and Tulaczyk, S.: A microbial
478 ecosystem beneath the West Antarctic ice sheet, *Nature*, 512, 310–313, <https://doi.org/10.1038/nature13667>,
479 2014.

480 Dow, C. F., Hubbard, A., Booth, A. D., Doyle, S. H., Gusmeroli, A., and Kulessa, B.: Seismic evidence of
481 mechanically weak sediments underlying Russell Glacier, West Greenland, *Ann. Glaciol.*, 54, 135–141,
482 <https://doi.org/10.3189/2013aog64a032>, 2013.

483 Engelhardt, H., Humphrey, N., Kamb, B., and Fahnestock, M.: Physical conditions at the base of a fast moving
484 Antarctic ice stream, *Science*, 248, 57–59, <https://doi.org/10.1126/science.248.4951.57>, 1990.

485 Filina, I. Y., Blankenship, D. D., Thoma, M., Lukin, V. V., Masolov, V. N., and Sen, M. K.: New 3D bathymetry
486 and sediment distribution in Lake Vostok: implication for pre-glacial origin and numerical modeling of the
487 internal processes within the lake, *Earth Planet. Sc. Lett.*, 276, 106–114,
488 <https://doi.org/10.1016/j.epsl.2008.09.012>, 2008.

489 Frezzotti, M., Tabacco, I. E., and Zirizzotti, A.: Ice discharge of eastern Dome C drainage area, Antarctica,
490 determined from airborne radar survey and satellite image analysis, *J. Glaciol.*, 46, 253–264,
491 <https://doi.org/10.3189/172756500781832855>, 2000.

492 Graves, R. W.: Simulating seismic wave propagation in 3D elastic media using staggered-grid finite differences,
493 *Bulletin of the seismological society of America*, 86, 1091–1106, <https://doi.org/10.1785/BSSA0860041091>,
494 1996.

495 Herron, D. A.: Pitfalls in seismic interpretation: depth migration artifacts, *The Leading Edge*, 19, 1016–1017,
496 <https://doi.org/10.1190/1.1438756>, 2000.

497 Horgan, H. J., Anandakrishnan, S., Jacobel, R. W., Christianson, K., Alley, R. B., Heeszel, D. S., Picotti, S., and
498 Walter, J. I.: Subglacial Lake Whillans — Seismic observations of a shallow active reservoir beneath a West
499 Antarctic ice stream, *Earth Planet. Sc. Lett.*, 331-332, 201–209, <https://doi.org/10.1016/j.epsl.2012.02.023>,
500 2012.

501 Isaaks, E. H. and Srivastava, R. M.: *An Introduction to Applied Geostatistics*, Oxford University Press, Oxford,
502 1989.

503 Johansen, T. A., Ruud, B. E., Bakke, N. E., Riste, P., Johannessen, E. P., and Henningsen, T.: Seismic profiling
504 on Arctic glaciers, *First Break*, 29, 65–71, <https://doi.org/10.3997/1365-2397.20112st1>, 2011.

505 Ju, H., Choi, Y., and Kang, S.-G.: Seismic Survey for the Subglacial Lake in Antarctica. *Geophysics and*
506 *Geophysical Exploration*, 27, 244–257. <https://doi.org/10.7582/gge.2024.27.4.244>, 2024.

507 Ju, H., Kang, S., Han, H., Beem, L. H., Ng, G., Chan, K., Kim, T., Lee, J., Lee, J., Kim, Y., and Pyun, S.:
508 Airborne and Spaceborne Mapping and Analysis of the Subglacial Lake D2 in David Glacier, Terra Nova
509 Bay, Antarctica. *J. Geophys. Res.: Earth Surf.*, 130, <https://doi.org/10.1029/2024jf008142>, 2025.

510 Kim, T., Han, H., Lee, H., and Ju, H.: Monitoring Subglacial Lake Activity in the David Glacier Region, East
511 Antarctica, Using a DInSAR Displacement Integration Approach, *IEEE J. Sel. Top. Appl. Earth Obs.*
512 *Remote Sens.*, 18, 22175–22192, <https://doi.org/10.1109/jstars.2025.3601588>, 2025.

513 King, E. C., Woodward, J., and Smith, A. M.: Seismic evidence for a water-filled canal in deforming till beneath
514 Rutford Ice Stream, West Antarctica, *Geophys. Res. Lett.*, 31, L20401,
515 <https://doi.org/10.1029/2004gl020379>, 2004.

516 Kirchner, J. F. and Bentley, C. R.: Seismic short-refraction studies on the Ross Ice Shelf, Antarctica, *J. Glaciol.*,
517 24, 313–319, <https://doi.org/10.3189/s0022143000014830>, 1979.

518 Kohnen, H.: The temperature dependence of seismic waves in ice, *J. Glaciol.*, 13, 144–147,
519 <https://doi.org/10.3189/s0022143000023467>, 1974.

520 Krail, P. M. and Shin, Y.: Deconvolution of a directional marine source, *Geophysics*, 55, 1542–1548,
521 <https://doi.org/10.1190/1.1442805>, 1990.

522 Lindzey, L. E., Beem, L. H., Young, D. A., Quartini, E., Blankenship, D. D., Lee, C.-K., Lee, W. S., Lee, J. I.,
523 and Lee, J.: Aerogeophysical characterization of an active subglacial lake system in the David Glacier
524 catchment, Antarctica, *Cryosphere*, 14, 2217–2233, <https://doi.org/10.5194/tc-14-2217-2020>, 2020.

525 Livingstone, S. J., Li, Y., Rutishauser, A., Sanderson, R. J., Winter, K., Mikucki, J. A., Björnsson, H., Bowling, J.
526 S., Chu, W., Dow, C. F., Fricker, H. A., McMillan, M., Ng, F. S. L., Ross, N., Siegert, M. J., Siegfried, M.,
527 and Sole, A. J.: Subglacial lakes and their changing role in a warming climate, *Nature Reviews Earth &*
528 *Environment*, 3, 106–124, <https://doi.org/10.1038/s43017-021-00246-9>, 2022.

529 Matsuoka, K., Skoglund, A., Roth, G., de Pomereu, J., Griffiths, H., Headland, R., Herried, B., Katsumata, K., Le
530 Brocq, A., Licht, K., Morgan, F., Neff, P., Ritz, C., Scheinert, M., Tamura, T., Van de Putte, A., van den
531 Broeke, M., von Deschwanden, A., Deschamps-Berger, C., ... Melvær, Y.: Quantarctica [Dataset].
532 Norwegian Polar Institute. <https://doi.org/10.21334/NPOLAR.2018.8516E961>, 2018.

533 Oliveira, M. S., Henriques, M. V. C., Leite, F. E. A., Corso, G., and Lucena, L. S.: Seismic denoising using
534 curvelet analysis, *Physica A*, 391, 2106–2110, <https://doi.org/10.1016/j.physa.2011.04.009>, 2012.

535 Peters, L. E., Anandakrishnan, S., Alley, R. B., and Smith, A. M.: Extensive storage of basal meltwater in the
536 onset region of a major West Antarctic ice stream, *Geology*, 35, 251–254, <https://doi.org/10.1130/g23222a.1>,
537 2007.

538 Picotti, S., Vuan, A., Carcione, J. M., Horgan, H. J., and Anandakrishnan, S.: Anisotropy and crystalline fabric of
539 Whillans Ice Stream (West Antarctica) inferred from multicomponent seismic data, *J. Geophys. Res. Sol.*
540 *Ea.*, 120, 4237–4262, <https://doi.org/10.1002/2014jb011591>, 2015.

541 Priscu, J. C. and Christner, B. C.: Earth's icy biosphere, in: *Microbial Diversity and Bioprospecting*, edited by:
542 Bull, A. T., ASM Press, Washington, D.C, 130–145, <https://doi.org/10.1128/9781555817770.ch13>, 2003.

543 Qin, L., Qiu, H., Nakata, N., Booth, A., Zhang, Z., Karplus, M., McKeague, J., Clark, R., and Kaip, G.: High-
544 resolution characterization of the firn layer near the West Antarctic ice sheet divide camp with active and
545 passive seismic data, *Geophys. Res. Lett.*, 51, e2024GL108933, <https://doi.org/10.1029/2024gl108933>, 2024.

546 Rignot, E., Mouginot, J., Scheuchl, B., van den Broeke, M., van Wessem, M. J., and Morlighem, M.: Four
547 decades of Antarctic Ice Sheet mass balance from 1979–2017, *P. Natl. Acad. Sci. USA*, 116, 1095–1103,
548 <https://doi.org/10.1073/pnas.1812883116>, 2019.

549 Robinson, E. A. and Treitel, S.: *Digital Imaging and Deconvolution*, Society of Exploration Geophysicists, Tulsa,
550 Okla, 2008.

551 Rose, K. E.: Characteristics of ice flow in Marie Byrd Land, Antarctica, *J. Glaciol.*, 24, 63–75,
552 <https://doi.org/10.3189/s0022143000014659>, 1979.

553 Schlegel, R., Brisbourne, A. M., Smith, A. M., Booth, A. D., Murray, T., King, E. C., and Clark, R. A.:
554 Subglacial bedform and moat initiation beneath Rutford Ice Stream, West Antarctica, *Geomorphology*, 458,
555 109207, <https://doi.org/10.1016/j.geomorph.2024.109207>, 2024.

556 Siegfried, M. R. and Fricker, H. A.: Thirteen years of subglacial lake activity in Antarctica from multi-mission
557 satellite altimetry, *Ann. Glaciol.*, 59, 42–55, <https://doi.org/10.1017/aog.2017.36>, 2018.

558 Siegfried, M. R., Venturelli, R. A., Patterson, M. O., Arnuk, W., Campbell, T. D., Gustafson, C. D., et al. (2023).
559 The life and death of a subglacial lake in West Antarctica. *Geology*, 51(5), 434–438.
560 <https://doi.org/10.1130/g50995.1>

561 Smith, A. M., Woodward, J., Ross, N., Bentley, M. J., Hodgson, D. A., Siegert, M. J., and King, E. C.: Evidence
562 for the long-term sedimentary environment in an Antarctic subglacial lake, *Earth Planet. Sc. Lett.*, 504, 139–
563 151, <https://doi.org/10.1016/j.epsl.2018.10.011>, 2018.

564 Smith, B. E., Fricker, H. A., Joughin, I. R., and Tulaczyk, S.: An inventory of active subglacial lakes in
565 Antarctica detected by ICESat (2003–2008), *J. Glaciol.*, 55, 573–595,
566 <https://doi.org/10.3189/002214309789470879>, 2009.

567 Smith, B. E., Fricker, H. A., Gardner, A. S., Medley, B., Nilsson, J., Paolo, F. S., Holschuh, N., Adusumilli, S.,
568 Brunt, K., Csatho, B., Harbeck, K., Markus, T., Neumann, T., Siegfried, M. R., and Zwally, H. J.: Pervasive
569 ice sheet mass loss reflects competing ocean and atmosphere processes, *Science*, 368, 1239–1242,
570 <https://doi.org/10.1126/science.aaz5845>, 2020.

571 Stearns, L. A., Smith, B. E., and Hamilton, G. S.: Increased flow speed on a large East Antarctic outlet glacier
572 caused by subglacial floods, *Nat. Geosci.*, 1, 827–831, <https://doi.org/10.1038/ngeo356>, 2008.

573 Thoma, M., Grosfeld, K., Smith, A. M., and Mayer, C.: A comment on the Equation of State and the freezing
574 point equation with respect to subglacial lake modelling, *Earth Planet. Sc. Lett.*, 294, 80–84,
575 <https://doi.org/10.1016/j.epsl.2010.03.005>, 2010.

576 Tulaczyk, S., Mikucki, J. A., Siegfried, M. R., Priscu, J. C., Barcheck, C. G., Beem, L. H., Behar, A., Burnett, J.,
577 Christner, B. C., Fisher, A. T., Fricker, H. A., Mankoff, K. D., Powell, R. D., Rack, F., Sampson, D.,
578 Scherer, R. P., and Schwartz, S. Y.: WISSARD at Subglacial Lake Whillans, West Antarctica: scientific
579 operations and initial observations, *Ann. Glaciol.*, 55, 51–58, <https://doi.org/10.3189/2014aog65a009>, 2014.

580 Voigt, D. E., Peters, L. E., and Anandakrishnan, S.: ‘Georods’: the development of a four-element geophone for
581 improved seismic imaging of glaciers and ice sheets, *Ann. Glaciol.*, 54, 142–148,
582 <https://doi.org/10.3189/2013aog64a432>, 2013.

583 Wingham, D. J., Siegert, M. J., Shepherd, A., and Muir, A. S.: Rapid discharge connects Antarctic subglacial
584 lakes, *Nature*, 440, 1033–1036, <https://doi.org/10.1038/nature04660>, 2006.

585 Winsborrow, M. C. M., Clark, C. D., and Stokes, C. R.: What controls the location of ice streams?, *Earth-Sci.
586 Rev.*, 103, 45–59, <https://doi.org/10.1016/j.earscirev.2010.07.003>, 2010.

587 Woodward, J., Smith, A. M., Ross, N., Thoma, M., Corr, H. F. J., King, E. C., King, M. A., Grosfeld, K., Tranter,
588 M., and Siegert, M. J.: Location for direct access to subglacial Lake Ellsworth: an assessment of geophysical
589 data and modeling, *Geophys. Res. Lett.*, 37, L11501, <https://doi.org/10.1029/2010gl042884>, 2010.

590 Wright, A. and Siegert, M.: A fourth inventory of Antarctic subglacial lakes, *Antarct. Sci.*, 24, 659–664,
591 <https://doi.org/10.1017/s095410201200048x>, 2012.

592 Yan, S., Blankenship, D. D., Greenbaum, J. S., Young, D. A., Li, L., Rutishauser, A., Guo, J., Roberts, J. L., van
593 Ommen, T. D., Siegert, M. J., and Sun, B.: A newly discovered subglacial lake in East Antarctica likely
594 hosts a valuable sedimentary record of ice and climate change, *Geology*, 50, 949–953,
595 <https://doi.org/10.1130/g50009.1>, 2022.

596 Yilmaz, Ö.: *Seismic Data Analysis: Processing, Inversion, and Interpretation of Seismic Data*, Society of
597 Exploration Geophysicists, Tulsa, Okla, 2001.

598 Zechmann, J. M., Booth, A. D., Truffer, M., Gusmeroli, A., Amundson, J. M., and Larsen, C. F.: Active seismic
599 studies in valley glacier settings: strategies and limitations, *J. Glaciol.*, 64, 796–810,
600 <https://doi.org/10.1017/jog.2018.69>, 2018.